Scripta Materialia 276 (2026) 117188

Contents lists available at ScienceDirect

Scripta Materialia

journal homepage: www.journals.elsevier.com/scripta-materialia

Solid -state dewetting in Pd/a-Ge bilayers

Bärbel Krause [a,*], Gregory Abadias [b], David Babonneau [b]

[a] Institut für Photonenforschung und Synchrotronstrahlung (IPS), Karlsruher Institut für Technologie, Karlsruhe, D-76021, Germany
[b] Institut PPrime, Département Physique et Mécanique des Matériaux, UPR 3346 CNRS, Université de Poitiers, TSA 41123, Poitiers Cedex 9, 986073, France

ARTICLE INFO

Keywords:
Dewetting
Real-time curvature measurement
Germanides
Sputter deposition
Solid-state reaction
Local epitaxy

ABSTRACT

The post-growth morphology and the chemical composition of sputter-deposited Pd/a-Ge films were studied by in situ atomic force microscopy and X-ray photoelectron spectroscopy under UHV conditions. The polycrystalline films consist of locally epitaxial Pd/Pd_2Ge grains on an amorphous germanium buffer layer. We found that the films show a thickness-dependent tendency for solid-state dewetting, which occurs at the interface between the Pd and Pd_2Ge layers and for Pd thicknesses below 6 nm. The post-growth dewetting is correlated with the real-time stress evolution during deposition. Real-time x-ray reflectivity measurements confirm that the dewetting is kinetically hindered during deposition, while individual grains dissolve after deposition, leaving deep holes. The room-temperature dewetting of Pd/a-Ge combines characteristic features of epitaxial and polycrystalline dewetting mechanisms. We propose that it is driven by the misfit strain between Pd and Pd_2Ge, while the stability of individual grains is determined by the local grain boundary configuration.

Thin films and multilayers are used for many applications, including quantum computing, sensors, solar cells, and protection layers. Independent of the application, the long-term stability and the interface quality are key figures determining the practical use of the layer systems. Thin film degradation via dewetting was therefore extensively studied for various thin film systems. In many cases, the dewetting processes can be described by continuum approaches [1–3]. The thermal dewetting of polycrystalline metal thin films, however, is strongly affected by the grain structure, i.e. the specific orientation and local environment of each grain. It was shown that the dewetting of polycrystalline films takes place by local grain dissolution and growth of (mainly, but not only) neighboring grains [4–6].

Dewetting as stress relaxation mechanism was extensively studied for epitaxial bilayer systems [7–9]. The solid-state-dewetting of polycrystalline bilayer systems, i.e. the impact of grain boundaries in addition to the stresses induced by the interface, is less well understood [10]. In the following, we will report on the solid-state dewetting in ultrathin, polycrystalline bilayer films. Specifically, we will demonstrate the correlation between stress evolution during deposition and a thickness-dependent tendency for post-growth dewetting at the polycrystalline but locally coherent Pd(111)/Pd_2Ge(111) interface which forms during deposition of Pd on amorphous Germanium (a-Ge) [11]. For this, we combine the results of *in situ* surface characterization studies of as-deposited bilayers (using the UHV cluster available at the KIT Light Source) with real-time information obtained during deposition, performed at the beamline SIXS of the Synchrotron Soleil (France). All samples were deposited using the same growth chamber.

Pd/a-Ge bilayers were deposited by magnetron sputtering without intentional substrate heating on 1 mm thick Silicon wafers covered by native oxide. For Ge deposition, an RF power of 30 W and a target-substrate distance of 129 mm were used. Pd was deposited by DC sputtering at 20 W and a target-substrate distance of 325 mm. The base pressure of the chamber was 2×10^{-6} Pa, the Ar pressure during deposition 0.37 Pa. The resulting deposition rates were 0.020 ± 0.001 nm/s for Pd, and 0.0495 ± 0.0020 nm/s for Ge. Under these conditions, the heating of the substrate due to the deposition itself is of the order of few degrees only, and we will refer to the substrate temperature as 'room temperature'. The surface after deposition was studied for a sample series with a 6.8 nm-thick Ge layer and a Pd thickness, h_{Pd}, varying between 1.2 and 9 nm. In the following, we will refer to a specific sample using the h_{Pd} value and (if needed) a consecutive number for repeated depositions with the same h_{Pd}. The as-deposited sample surface was characterized *in situ* by non-contact Atomic Force Microscopy (AFM) and X-ray Photoelectron Spectroscopy (XPS) measurements. Height distributions and roughness values (σ^{post}, extracted by a Gaussian fit from the height distribution) were determined from AFM images with the size 1000×1000 nm^2 and 400×400 data points. For the roughness, an error of 10 % was assumed. To highlight special features of the morphology, zoomed-in images with the size 500×500 nm^2 were recorded. The AFM images were plotted using the free software WSxM [12]. The

* Corresponding author.
E-mail address: baerbel.krause@kit.edu (B. Krause).

https://doi.org/10.1016/j.scriptamat.2026.117188
Received 9 November 2025; Received in revised form 14 January 2026; Accepted 20 January 2026
Available online 29 January 2026

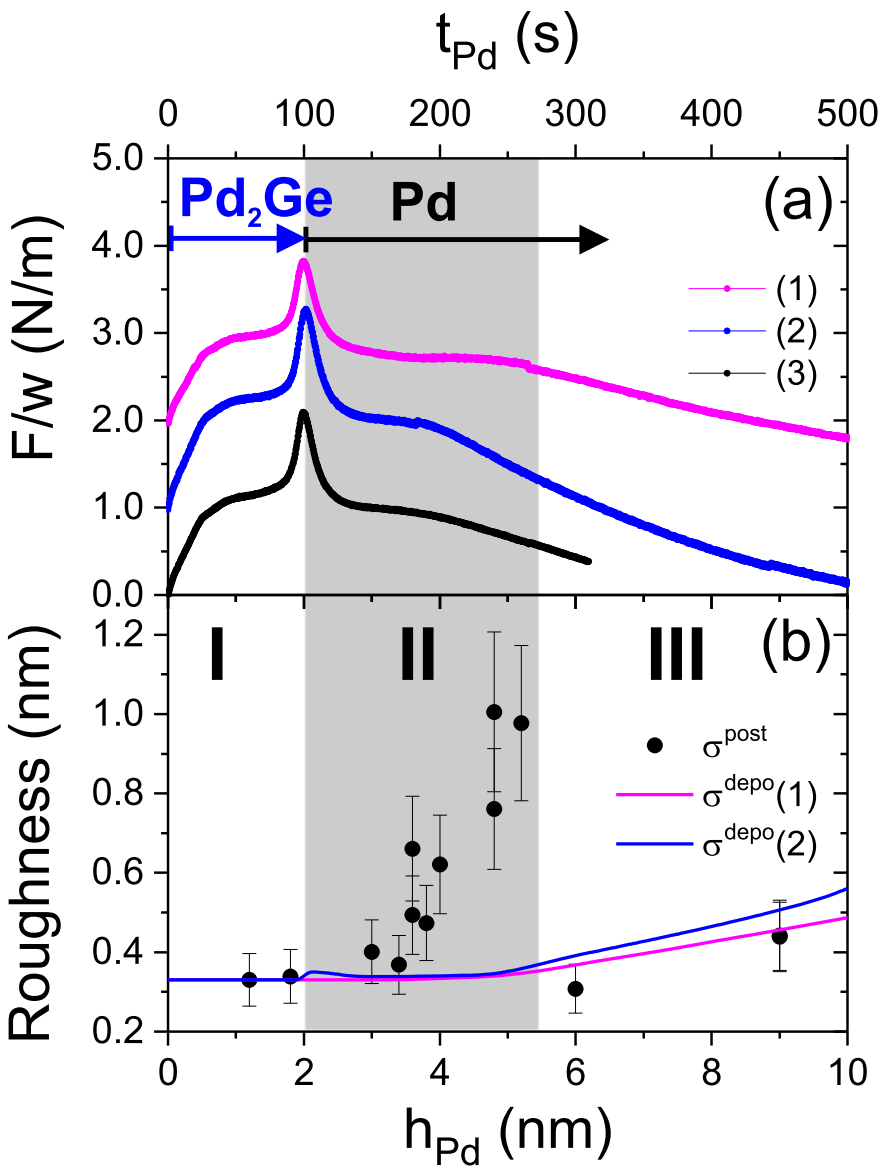

Fig. 1. (a) Real-time stress evolution during deposition of Pd on amorphous germanium. For clarity, the curves corresponding to 3 different samples are vertically shifted. (b) Real-time (lines) and post-growth (black circles) roughness at different h_{Pd}.

image analysis was performed with Matlab. Complementary information about the real-time evolution of the roughness, σ^{depo}, was obtained with a precision of $\pm 0.01 - 0.02$ nm from X-ray reflectivity (XRR) measurements during Pd/a-Ge deposition on 100 μm thin silicon substrates covered by native oxide. Simultaneously, the stress state during deposition was monitored by optical curvature measurements. The force per unit width (F/w), which is equivalent to the stress × thickness product, was calculated from the thickness and the elastic properties of the substrate using the Stoney equation. The slope of F/w corresponds to the incremental stress, s_i, which represents the stress change per deposited volume. Further information about the deposition conditions and the sample characterization, including a detailed example for the extraction of roughness values from real-time XRR, can be found in [11].

Fig. 1 relates the stress evolution during deposition to the thickness-dependent morphology during and after deposition, using the roughness as indicator for morphology changes. Fig. 1(a) presents repeated measurements of the real-time F/w curves during Pd deposition on a-Ge. In all cases, Pd_2Ge forms up to the F/w peak at $h_{Pd} = 2$ nm (region I) and is then covered by Pd. The characteristic tensile peak originates from the crystallization of an initially amorphous Pd_2Ge layer. During further Pd deposition, an F/w plateau is observed (region II with $s_i \approx 0$), followed by compressive growth ($s_i < 0$) in region III with $h_{Pd} \geq 6.0$ nm. The stress evolution close to the interface ($h_{Pd} < 3nm$) is highly reproducible. It is related to the interface formation and was discussed elsewhere [11]. During further deposition, the data are qualitatively similar, but the length of the plateau and the slope in the compressive region vary from sample to sample.

The F/w evolution is correlated with the roughness evolution shown in Fig. 1(b). For two of the stress curves, the simultaneously measured roughness, σ^{depo}, is shown as line in the respective color. In the regions I and II, σ^{depo} is close to the substrate roughness (≈ 0.33 nm). In region III, σ^{depo} increases slowly but does not exceed 0.6 nm. The post-growth roughness, σ^{post}, is shown as dots. Close to the interface (region I) and during later growth (region III), σ^{post} agrees with σ^{depo}. In the plateau region, however, σ^{post} increases with increasing h_{Pd}. The maximum roughness of 1 nm is obtained after deposition of $h_{Pd} \approx 5$ nm. This coincides with the maximum extent of the F/w plateau. The difference between σ^{depo} and σ^{post} can only be explained by post-growth morphology changes occurring in region II.

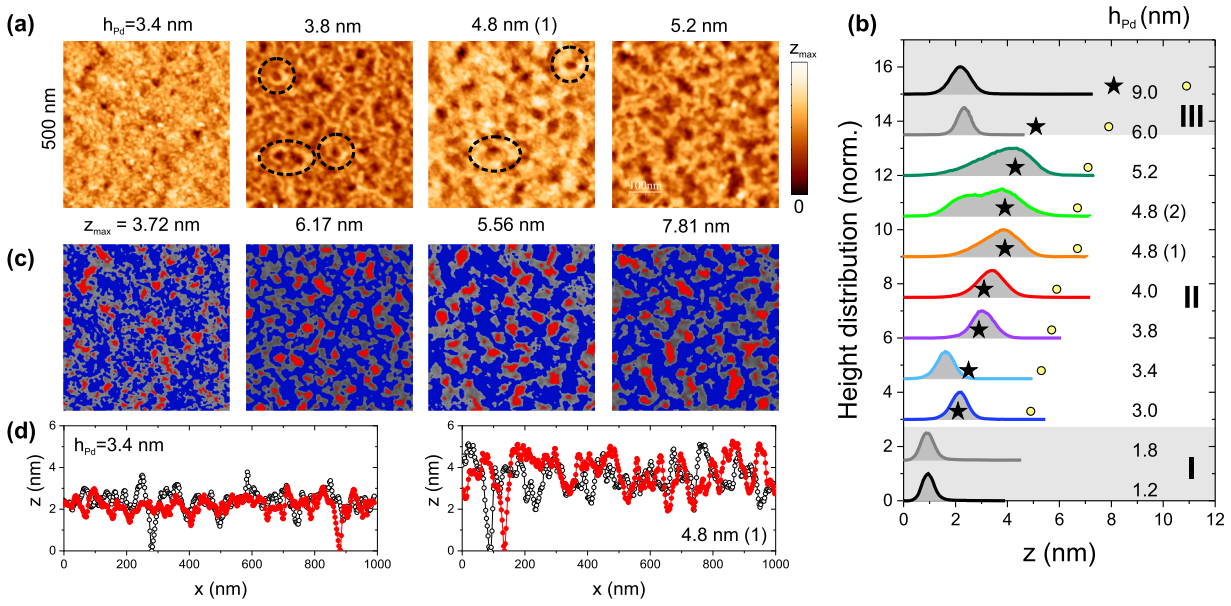

Fig. 2. (a) Examples for the morphology of Pd/a-Ge samples in the intermediate thickness region (image size 500×500 nm^2, for the corresponding 1×1 μm^2 images see supplementary material, Fig. S1). All images use the same color scale but have different z_{max}. The samples show characteristic holes, often surrounded by ridges (dashed circles). (b) Height distribution of 1×1 μm^2 AFM images with different h_{Pd}. For clarity, the curves are vertically shifted. The stars mark the expected position, z^*, of the surface in region II and III, assuming dewetting at the Pd/Pd_2Ge interface. The dots were calculated assuming dewetting at the Pd_2Ge/a-Ge interface. The Pd_2Ge interlayer forms reactively and is completed at $h_{Pd} = 2.0$ nm, corresponding to a Pd_2Ge thickness of 3.0 nm. The threshold images in (c) enhance the structure evolution. Red regions with $z < \langle z \rangle - 1.5\sigma^{post}$ correspond to deep holes. The blue, interconnected regions are elevated with $z > \langle z \rangle$. Fig. S2 (supplementary material) shows the same images with a constant threshold of ±0.4 nm. (d) AFM line scans crossing deep holes after deposition of different amounts of Pd.

Fig. 2(a) shows AFM images typical for region II, revealing the origin of the roughness increase. Compared to the surfaces in region I (germanide formation) and III (thick Pd layers), which are characterized by densely packed clusters with a typical size of 20–30 nm [11], the surface in region II is less homogeneous: The cluster size varies from 10 to 50 nm, and deep holes with a typical diameter around 40 nm are visible, often surrounded by ridges (e.g., encircled regions). The corrugation increases with h_{Pd}. This morphology is known from thermal dewetting of polycrystalline thin films. Selected line scans in Fig. 2(d) visualize the difference between average surface height and local hole depth for $h_{Pd} = 3.4$ nm and $h_{Pd} = 4.8$ nm (1).

The height distributions extracted from the AFM images are shown in Fig. 2(b). They allow for comparing the average surface height, $\langle z \rangle$, and the depth of the holes. $z = 0$ is given by the lowest point within the scanned region. The surfaces in region I and III, which are not affected by the dewetting process, have a Gaussian height distribution. Without hole formation, $\langle z \rangle$ is comparably low (1 nm during Pd_2Ge deposition in region I, and 2 nm during later growth in region III). In region II, the height distribution shifts continuously to higher values and becomes increasingly asymmetric. Surprisingly, the height profiles of two repeated depositions, $h_{Pd} = 4.8$ nm (1) and (2), are different. 4.8 nm (2) is the only height profile with two maxima. The corresponding AFM image and the XPS spectra of 4.8 nm (1) and (2) are shown in Fig. 3. In agreement with the different morphologies, the Pd 3d 5/2 spectrum of 4.8 nm (1) shows the characteristic asymmetric spectrum of metallic Pd, while the spectrum of 4.8 nm (2) is broadened due to coexisting Pd-Ge and Pd-Pd components (Fig. 3(b)). We attribute the first maximum of the height distribution to uncovered Pd_2Ge areas (explaining the Pd-Ge component of the XPS signal), and the higher maximum to areas covered by metallic Pd (in agreement with the Pd-Pd component of the XPS signal). It seems that the different XPS signals of the samples 4.8 nm (1) and (2) reflect a different degree of solid-state dewetting at the Pd/Pd_2Ge interface. To verify this assumption, we have compared the measured height distributions with the expected Pd layer thickness. For each sample, the lowest data point within the measured region determines the shift of the peak position. Assuming that the holes in the dewetting region reach down to the Pd/Pd_2Ge interface, we have calculated the surface height, z^*, expected for a homogeneous Pd layer:

$$z^* = z_{ref} + h_{Pd} - h^0_{Pd}. \quad (1)$$

For $h_{Pd} \leq h^0_{Pd} = 2.0$ nm, Pd is converted to Pd_2Ge. The morphology during Pd_2Ge formation does not change significantly, as confirmed by the height distributions at $h_{Pd} = 1.2$ nm and $h_{Pd} = 1.8$ nm. Therefore, we use $z_{ref} = \langle z(h_{Pd} = 1.8\ \text{nm}) \rangle$ as reference for the Pd/Pd_2Ge interface. z^* is shown as stars in Fig. 2(b). The maximum of the measured height distributions is close to the height expected for a homogeneous Pd layer on the Pd_2Ge interlayer, confirming that at least some of the holes reach down to (or close to) the Pd/Pd_2Ge interface. An alternative calculation was performed, assuming dewetting at the Pd_2Ge/a-Ge interface (dots). Compared to the stars, these values are increased by 3.0 nm, i.e. the Pd_2Ge thickness. This scenario can be excluded since the calculated values differ by several nm from the maximum of the height distribution. Small deviations between expected and calculated values, as e.g. found for $h_{Pd} = 3.4$ nm and $h_{Pd} = 4.0$ nm, are attributed to the small number of deep holes in the measured area, resulting in statistical errors.

The holes are better visible in the threshold images extracted from the 500×500 nm^2 AFM images (Fig. 2(c)), where areas with $z < \langle z \rangle - 1.5\sigma^{post}$ are shown in red. The meander-like structures formed by areas with z above (blue areas) and below (grey + red areas) the average surface height are typical for the dewetting region. With increasing h_{Pd}, the number of holes decreases, and the typical length scales (hole diameter, meander diameter) increase.

Our results reveal a thickness-dependent tendency for solid-state dewetting of ultrathin Pd layers deposited at room temperature on a-Ge. The post-growth dewetting occurs only for h_{Pd} values in the plateau region of the real-time F/w curve, i.e., post-growth dewetting is only observed in a thickness region where the incremental stress during deposition is near 0. The surface roughness is a clear indicator of the morphology change. As shown in Fig. 1(b), the dewetting during deposition is kinetically hindered. The roughness increase occurs only af-

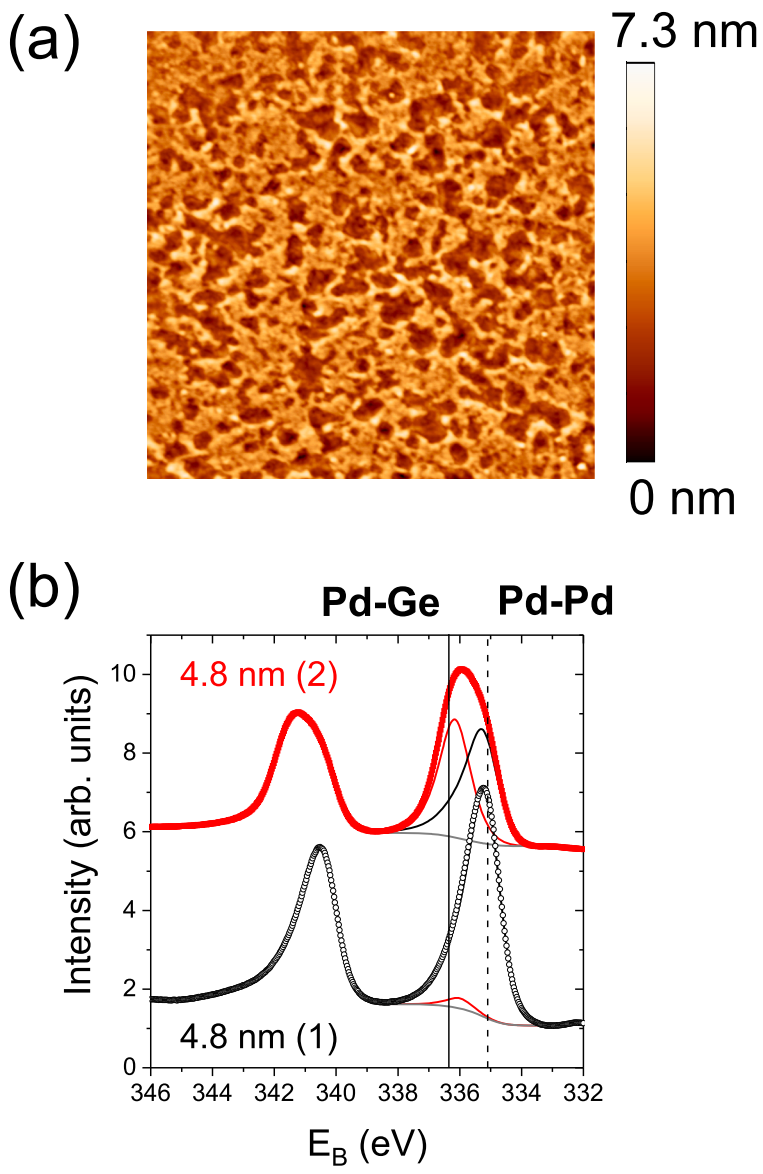

Fig. 3. (a) AFM image of the sample (2) with $h_{Pd} = 4.8$ nm (image size 1000×1000 nm^2). (b) XPS spectra of the samples (1) and (2) with $h_{Pd} = 4.8$ nm (black and red symbols). The Shirley background and the fitted Pd-Pd and Pd-Ge components are shown as gray, red and black lines. The expected peak positions for the Pd-Pd and the Pd-Ge bond are indicated by solid and dashed vertical lines, respectively.

ter growth interruption. It originates from the local dissolution of Pd grains, leaving holes that reach down to the Pd_2Ge interlayer. As expected for solid-state dewetting, the density of holes decreases with increasing Pd thickness [1]. When h_{Pd} exceeds the F/w plateau region, the Pd film remains stable. This is in agreement with previous studies of solid-state dewetting. Various polycrystalline, thin metal films of $10 - 40$ nm thickness were reported to be stable at room temperature, but dewetting could be induced by a temperature increase of the order of 100 K [4,5,10]. Sputter-deposited, ultrathin Ag layers on silicon covered by native oxide, e.g., were found to be continuous after deposition, but dewetted at elevated temperatures. The homologous temperature, T/T_m, i.e. the temperature normalized to the melting point T_m of a material, is a measure for self-diffusion. The room-temperature values for Pd and Ag are 0.15 and 0.22 [13]. Thus, solid-state dewetting of a continuous film at room temperature should be less likely for Pd than for Ag. Furthermore, it was found that a Ge buffer layer facilitates the formation of continuous Ag layers at few nm thickness [14]. Pd interacts much stronger than Ag with Ge, forming even compounds and locally epitaxial bilayer grains. Therefore, the observed dewetting of Pd at room temperature seems to be surprising.

In the following, we will discuss our findings in the context of the dewetting models summarized in Fig. 4. Fig. 4(a) visualizes the post-growth dewetting of epitaxial, Fig. 4(b) the post-growth dewetting of polycrystalline thin films. The solid-state dewetting after Pd deposition on a-Ge occurs at the coherent Pd/Pd_2Ge interface, combining therefore characteristics of epitaxial and polycrystalline solid-state dewetting, as schematically shown in Fig. 4(c). Based on our experimental observations, we consider the post-growth dewetting without wetting layer (Volmer-Weber growth). Without deposited flux F, and assuming a sufficiently high mobility of the atoms, dewetting can occur at $h_c = 0$ nm. Dewetting during deposition occurs for layers above a flux and temperature-dependent critical thickness, $h > h_c(F,T)$. As shown in Fig. 4, post-growth dewetting is possible for $h < h_c(F,T)$.

Dewetting is driven by the reduction of the Gibbs free energy, ΔG, with

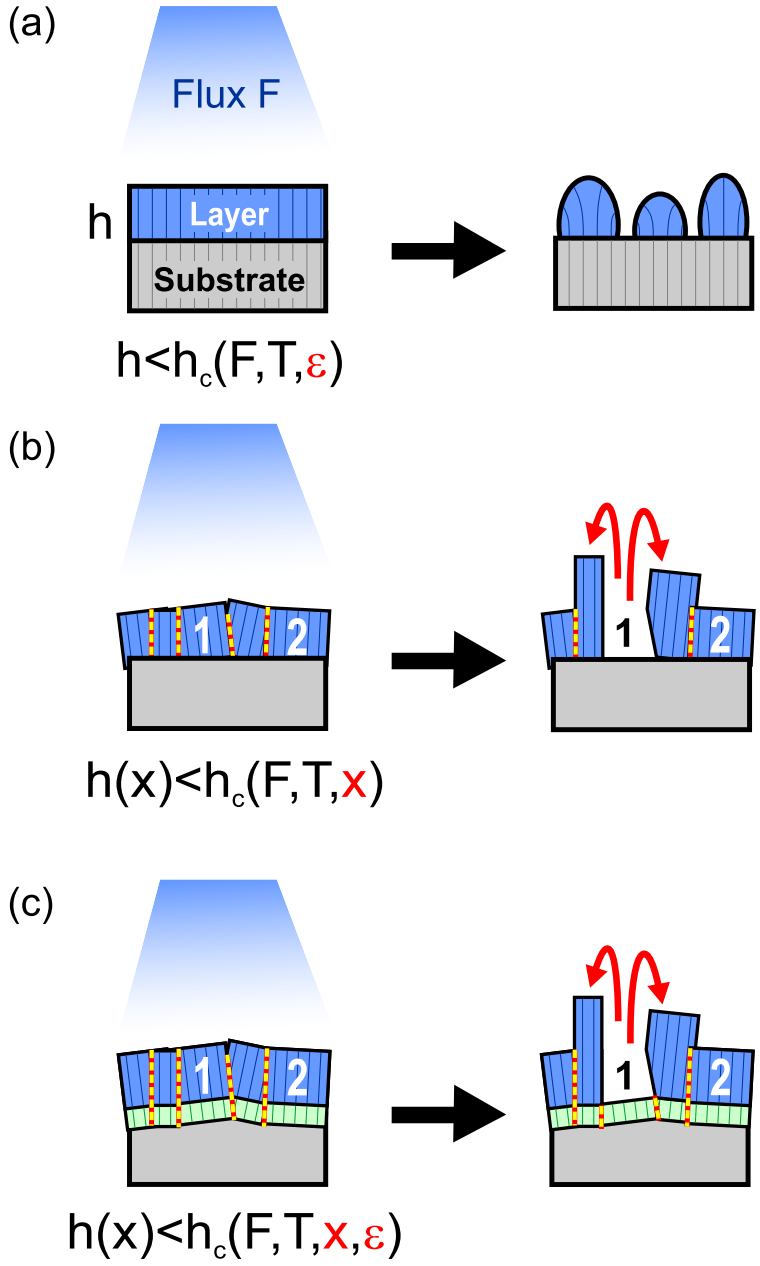

Fig. 4. Post-growth solid-state dewetting for (a) epitaxial, (b) polycrystalline, and (c) locally epitaxial thin films. The critical thickness, h_c, for dewetting during deposition depends on the flux F and the temperature T. In case of epitaxial thin films, it is also affected by the lattice strain, ϵ. Due to the locally different grain boundaries (dashed yellow/red lines), the critical thickness of polycrystalline films is position-dependent (x being the position). Thus, grain 1 dissolves after deposition while grain 2 with different grain boundary orientations remains unchanged. For locally epitaxial films, both contributions, x and ϵ, are relevant.

$$\Delta G = \Delta G_{s/i} + \Delta G_{GB} + \Delta G_{el}. \tag{2}$$

The geometry changes during the dewetting process affect the surface and interface contributions, summarized in $\Delta G_{s/i}$, and reduce the total grain boundary energy, ΔG_{GB}. In case of epitaxial films (Fig. 4(a)), the reduction of the elastic energy ΔG_{el} due to the lattice mismatch is dominant. The elastic energy increases with increasing film thickness and can be reduced by different mechanisms, including grain rotation , dislocation formation, twinning, and dewetting [1,7,15]. Dewetting is favored at low film thicknesses and large lattice mismatch, i.e. the critical thickness for dewetting in epitaxial systems, $h_c(F,T,\epsilon)$, depends on the lattice strain, ϵ. Dewetting (i.e., quantum dot formation) during and after deposition can occur for nm-scale semiconductor layers with a lattice mismatch $\gtrsim 2\%$ [7]. As previously reported, we found strong indications for local epitaxial growth of Pd on a Pd_2Ge template [11]. For the coherent growth of Pd(111) on $Pd_2Ge(111)$ with the proposed in plane orientation $Pd_2Ge[1\bar{1}0] \parallel Pd[1\bar{1}0]$, the lattice mismatch is comparatively large (5.6 % with respect to Pd along $Pd[1\bar{1}0]$). Thus, the reduction of the elastic energy can explain the dewetting at the Pd/Pd_2Ge interface. Recent simulations based on continuum models propose that strain accelerates the dewetting process [16]. The observed dewetting of only few nm thin Pd layers on Pd_2Ge already at room temperature, which is also the deposition temperature, is in agreement with this conclusion.

In case of polycrystalline films, the grain boundary energy is assumed to be most relevant. It depends on the grain size and increases with the angle between adjacent grains, leading to a position-dependent Gibbs free energy. This results in a position-dependent critical thickness, $h_c(F,T,x)$. The dewetting of a polycrystalline film is visualized in Fig. 4(b). Grain boundaries act as surface diffusion barriers [17], imped-

ing the inter-grain diffusion required for dissolution of grains. Annealing enhances the inter-grain diffusion, enabling the dissolution of unfavorable grains with large-angle grain boundaries. The material is added to more favorable grains, which leads to a characteristic inhomogeneous morphology [2,18]. For Pd/a-Ge, we have found typical signs for grain dissolution. We suggest therefore that both contributions (grain boundary and misfit strain) contribute to the dewetting process. Thus, the critical thickness, $h_c(F,T,x,\epsilon)$, depends on lattice mismatch and position. Close to the interface, we assume a Pd grain density given by the Pd_2Ge template, as shown in Fig. 4(c). ΔG_{GB} and ΔG_{el} increase with the film thickness, i.e. the driving force for dewetting increases. ΔG_{el} as a volume effect drives the dewetting process, but the local grain boundary energy, $\Delta G_{GB}(x)$, determines the probability for dissolution of a specific grain. The dewetting is observed only in region II, indicating that other relaxation or growth mechanisms dominate the later growth stages.

Interestingly, the post-growth dewetting occurs in a thickness region where the F/w signal during deposition is nearly constant. For epitaxially strained films with $h < h_c(F,T,\epsilon)$, a constant slope during deposition would be expected, with negative slope for $a_F > a_S$ and positive slope for $a_F < a_S$, a_F and s_S being the lattice parameters of film and substrate. However, in case of polycrystalline thin films, lattice mismatch is only one of many contributions to the total stress [19]. The F/w plateau might be related to superposed effects, e.g. a tensile incremental stress due to the local epitaxy, and a compressive incremental stress due to point defects. Competing mechanisms of stress build-up and relaxation, sensitive to tiny changes in the growth conditions and local defect density, would explain the slightly different lengths of the F/w plateau during repeated depositions. Eventually we find that the F/w plateau is clearly correlated with the occurrence of post-growth dewetting, but its origin remains ambiguous due to the complexity of the system.

We have shown that dewetting processes in locally epitaxial systems can occur within few nm of the interface, in analogy to the quantum dot formation in epitaxial systems. The discrepancy between post-growth and real-time roughness evolution indicates a kinetically hindered dewetting process. Solid-state dewetting in polycrystalline layers is strongly affected by the local microstructure, and its control is therefore even more challenging than the control of epitaxial quantum dot formation.

CRediT authorship contribution statement

Bärbel Krause: Writing – original draft, Investigation, Formal analysis, Conceptualization; **Gregory Abadias:** Writing – review & editing, Investigation, Formal analysis; **David Babonneau:** Writing – review & editing, Investigation.

Data availability

Data will be made available on request.

Declaration of competing interest

The authors declare that they have no known competing financial interests or personal relationships that could have appeared to influence the work reported in this paper.

Acknowledgements

We acknowledge the synchrotron radiation source SOLEIL for the provision of beam-time within the standard proposal 20191667. We would like to thank the team of the beamline SIXS, Alessandro Coati, Yves Garreau, Andrea Resta, Alina Vlad, and Benjamin Voisin, for assistance in using beamline, and acknowledge the general support of the synchrotron staff. We are grateful for the support at the UHV Analysis Laboratory (KIT/IPS), provided by Annette Weißhardt. This work pertains to the French Government programs “Investissements d’Avenir” (EUR INTREE, reference ANR-18-EURE-0010) and LABEX INTERACT-IFS (reference ANR-11-LABX-0017-01).

Appendix A. Supporting material

The threshold analysis of selected 1×1 μm^2 AFM images is presented in Fig. S1 of the supporting material. An alternative threshold-analysis of the 500×500 nm^2 images, using a fixed threshold of ± 0.4 nm, is presented in Fig. S2.

Supplementary material

Supplementary material associated with this article can be found, in the online version, at 10.1016/j.scriptamat.2026.117188

References

[1] C.V. Thompson, Solid-state dewetting of thin films, Annu. Rev. Mater. Res. 42 ((2012) 399–434. https://www.annualreviews.org/content/journals/10.1146/annurev-matsci-070511-155048. https://doi.org/10.1146/annurev-matsci-070511-155048

[2] F. Leroy, L. Borowik, F. Cheynis, Y. Almadori, S. Curiotto, M. Trautmann, J.C. Barbé, P. Müller, How to control solid state dewetting: a short review, Surf. Sci. Rep. 71 (2) (2016) 391–409. https://www.sciencedirect.com/science/article/pii/S0167572916300012. https://doi.org/10.1016/j.surfrep.2016.03.002

[3] J. Ye, D. Zuev, S. Makarov, Dewetting mechanisms and their exploitation for the large-scale fabrication of advanced nanophotonic systems, Int. Mater. Rev. 64 (8) (2019) 439–477. https://doi.org/10.1080/09506608.2018.1543832

[4] S. Jahangir, X. Cheng, H.H. Huang, J. Ihlefeld, V. Nagarajan, In-situ investigation of thermal instabilities and solid state dewetting in polycrystalline platinum thin films via confocal laser microscopy, J. Appl. Phys. 116 (16) (2014) 163511. https://pubs.aip.org/aip/jap/article-pdf/doi/10.1063/1.4898691/13939601/163511_1_online.pdf https://doi.org/10.1063/1.4898691

[5] P. Jacquet, R. Podor, J. Ravaux, J. Teisseire, I. Gozhyk, J. Jupille, R. Lazzari, Grain growth: the key to understand solid-state dewetting of silver thin films, Scr. Mater. 115 (2016) 128–132. https://www.sciencedirect.com/science/article/pii/S1359646216300100. https://doi.org/10.1016/j.scriptamat.2016.01.005

[6] P. Jacquet, R. Podor, J. Ravaux, J. Lautru, J. Teisseire, I. Gozhyk, J. Jupille, R. Lazzari, On the solid-state dewetting of polycrystalline thin films: capillary versus grain growth approach, Acta Mater. 143 (2018) 281–290. https://www.sciencedirect.com/science/article/pii/S1359645417306572. https://doi.org/10.1016/j.actamat.2017.08.070

[7] V.G. Dubrovskii, Nucleation Theory and Growth of Nanostructures, NanoScience and Technology, Springer Heidelberg New York Dordrecht London, 2014.

[8] C. Wansorra, E. Bruder, W. Donner, Atomistic view onto solid state dewetting: thin bismuth films with and without strain gradient, Acta Mater. 200 (2020) 455–462. https://www.sciencedirect.com/science/article/pii/S1359645420307242. https://doi.org/10.1016/j.actamat.2020.09.030

[9] M. Levi, A. Bisht, E. Rabkin, Diffusion-induced recrystallization during the early stages of solid-state dewetting of Ni-Pt bilayers, Acta Mater. 225 (2022) 117537. https://www.sciencedirect.com/science/article/pii/S1359645421009150. https://doi.org/10.1016/j.actamat.2021.117537

[10] F. Li, D. Flock, D. Wang, P. Schaaf, Solid-state dewetting of Ag/Ni bi-layers: accelerated void formation by the stress gradient in the bottom Ni layer, J. Alloys Compd. 960 (2023) 170735. https://www.sciencedirect.com/science/article/pii/S0925838823020388. https://doi.org/10.1016/j.jallcom.2023.170735

[11] B. Krause, G. Abadias, D. Babonneau, A. Michel, A. Resta, A. Coati, Y. Garreau, A. Vlad, A. Plech, P. Wochner, T. Baumbach, In situ study of the interface-mediated solid-state reactions during growth and postgrowth annealing of Pd/a-Ge bilayers, ACS Appl. Mater. Interfaces 15 (8) (2023) 11268–11280. PMID: 36791093, https://doi.org/10.1021/acsami.2c20600

[12] I. Horcas, R. Fernández, J.M. Gómez-Rodríguez, J. Colchero, J. Gómez-Herrero, A.M. Baro, WSXM: a software for scanning probe microscopy and a tool for nanotechnology, Rev. Sci. Instrum. 78 (1) (2007) 013705. https://pubs.aip.org/aip/rsi/article-pdf/doi/10.1063/1.2432410/13579366/013705_1_online.pdf https://doi.org/10.1063/1.2432410

[13] B. Predel, Landolt-Börnstein - Group IV Physical Chemistry 12A, Springer-Verlag Berlin Heidelberg, 2006. Copyright 2006 Springer-Verlag Berlin Heidelberg, https://materials.springer.com/lb/docs/sm_lbs_978-3-540-33962-5_2. https://doi.org/10.1007/10793176_2

[14] E. Jeong, G. Zhao, S.M. Yu, S.-G. Lee, J.-S. Bae, J. Park, J. Rha, G.-H. Lee, J. Yun, Minimizing optical loss in ultrathin ag films based on ge wetting layer: insights on Ge-mediated Ag growth, Appl. Surf. Sci. 528 (2020) 146989. https://www.sciencedirect.com/science/article/pii/S0169433220317463. https://doi.org/10.1016/j.apsusc.2020.146989

[15] M. Levi, A. Bisht, C. Chatelier, C. Atlan, J. Eymery, S. Leake, P. Boesecke, M.-I. Richard, E. Rabkin, Giant transformation strain and rotation in Ni-Pt nanoparticles caused by atomic ordering, Acta Mater. 294 (2025) 121129. https://www.sciencedirect.com/science/article/pii/S1359645425004173. https://doi.org/10.1016/j.actamat.2025.121129

[16] F. Boccardo, F. Rovaris, A. Tripathi, F. Montalenti, O. Pierre-Louis, Stress-induced acceleration and ordering in solid-state dewetting, Phys. Rev. Lett. 128 (2022) 026101. https://link.aps.org/doi/10.1103/PhysRevLett.128.026101. https://doi.org/10.1103/PhysRevLett.128.026101

[17] S. Mahieu, P. Ghekiere, D. Depla, R. De Gryse, Biaxial alignment in sputter deposited thin films, Thin Solid Films 515 (4) (2006) 1229–1249. https://www.sciencedirect.com/science/article/pii/S004060900600784X. https://doi.org/10.1016/j.tsf.2006.06.027

[18] J. Gao, A. Malchère, S. Yang, A. Campos, T. Luo, K. Quertite, P. Steyer, C. Girardeaux, L. Zhang, D. Mangelinck, Dewetting of Ni silicide thin film on Si substrate: In-situ experimental study and phase-field modeling, Acta Mater. 223 (2022) 117491. https://www.sciencedirect.com/science/article/pii/S1359645421008697. https://doi.org/10.1016/j.actamat.2021.117491

[19] G. Abadias, E. Chason, J. Keckes, M. Sebastiani, G.B. Thompson, E. Barthel, G.L. Doll, C.E. Murray, C.H. Stoessel, L. Martinu, Review article: stress in thin films and coatings: current status, challenges, and prospects, J. Vac. Sci. Technol. A 36 (2) (2018) 020801. https://doi.org/10.1116/1.5011790